发 光 学 报
CHINESE JOURNAL OF LUMINESCENCE

Article ID: 1000-7032(XXXX)XX-0001-13

Distinct Thermal Quenching of Upconversion and Downshifting Luminescence Caused by Dynamic Defects in Ion-conductive $Na_3Sc_2(PO_4)_3$: Yb^{3+}, Er^{3+} Phosphor

WANG Shijie, WANG Yinghan, TAO Zhengren, AN Zhengce, YE Shi*

(*Key Laboratory of Fiber Laser Materials and Applied Techniques, School of Materials Science and Engineering, South China University of Technology, Guangzhou* 510641, *China.*)

* *Corresponding Author, E-mail: msyes@scut. edu. cn*

Abstract: Eu^{2+}-doped $Na_3Sc_2(PO_4)_3$ ionic conductor possesses superior thermal quenching (TQ) resistance, which is considered as a promising phosphor for high-power lighting applications. Yet the underlying mechanism of negative thermal quenching (NTQ) is not fully understood. In this study, we focus on upconversion (UC) and downshifting (DS) luminescence of Yb^{3+}/Er^{3+} with *f*–*f* transition rather than susceptible *d*–*f* transition of Eu^{2+} in $Na_3Sc_2(PO_4)_3$, aiming to get a more insightful view. The results show that thermally accelerated dynamic defects/ions contributes to the significant negative thermal quenching (NTQ) of UC luminescence and thermally stabilized DS luminescence by promoting the radiative transition and suppressing the non-radiative transition. The UC process with slow population rate is more susceptible to perturbation of Na^+ migration process with time scale equivalent to that of the former, resulting in evident NTQ of UC luminescence. This research opens an avenue for understanding the NTQ mechanism of luminescence via dynamic defects/ions.

Key words: $Na_3Sc_2(PO_4)_3$: Yb^{3+}, Er^{3+}; Upconversion Luminescence; Downshifting Luminescence; Negative thermal quenching; Energy transfer

CLC number: Document **Document code**: **DOI**: 10. 37188/CJL. 20240073

动态缺陷导致 $Na_3Sc_2(PO_4)_3$:Yb^{3+},Er^{3+}材料上转换和下转移发光不同热猝灭行为的研究

汪世杰, 王映涵, 陶正仁, 安正策, 叶柿*

(华南理工大学, 材料科学与工程学院, 发光材料与器件国家重点实验室, 广东省光纤激光材料与应用技术重点实验室, 广东 广州 510641)

摘要: 掺 Eu^{2+} 的离子导体 $Na_3Sc_2(PO_4)_3$具有优异的抗热猝灭性能, 是一种很有前景的大功率照明用发光材料。然而, 其负热猝灭的机理仍有待深入研究。本文以 Yb^{3+}/Er^{3+}的*f*–*f*跃迁上转换和下转移窄带发射而非更易受干扰的 Eu^{2+}*d*–*f*跃迁发射为研究对象, 旨在获得更清晰的机理。结果表明, 热致缺陷/离子的动态迁移能促进高温下辐射跃迁和抑制非辐射跃迁, 导致了上转换发光具有显著的负热猝灭, 下转移发光热猝灭较小。其中, 布居速率较慢的上转换过程更容易受到时间尺度与之相当的 Na^+/空位迁移过程的影响。本研究研究可为理解发光材料热猝灭机制提供另一种视角。

关 键 词: $Na_3Sc_2(PO_4)_3$: Yb^{3+}, Er^{3+}; 上转换发光; 下转移发光; 负热猝灭; 能量传递

收稿日期: XXXX-XX-XX; **修订日期**: XXXX-XX-XX
基金项目: 国家自然科学基金(520712126)
Supported by National Natural Science Foundation of China(520712126)

1 Introduction

The phenomenon of decreased luminescence intensity of a phosphor with elevated temperature is the so-called TQ. TQ is the non-radiative relaxation of electrons from the excited state to the ground state owing to various causes[1], which could significantly affect the performance of optoelectronic devices[2-6]. Many strategies have been proposed to combat TQ, including but not limited to defect engineering[7-9], energy transfer[10], structural modulations[11-13], layer structure design[14], negative thermal expansion[15-16], surface coating[17], glass technology[18], etc. Significantly, TQ depends on structure of the matrix to some extent[19]. Thus, materials with a dense structure and high structural stiffness are often designed to achieve TQ resistance or even NTQ of luminescence[20-21].

Phosphates are promising materials in resisting TQ due to their favorable structural stiffness and dense composition. $Na_3Sc_2(PO_4)_3$ (NSP) compound was reported in the 1980s and has been developed as an ionic conductor material since then[22-23]. Wang et al. presented the NSP: Eu^{2+} phosphor with an excellent TQ resistance, high photoluminescence quantum yield (PLQY), and high color purity, making it superior to the commercial $BaMgAl_{10}O_{17}$: Eu^{2+} phosphor. They attributed the thermal enhancement of luminescence to traps caused by substitution via non-equivalent ions[24]. Won Bin Im et al. investigated the TQ resistance of NSP: Eu^{2+} from room temperature to 250°C and claimed that it was due to thermally induced structural transitions associated with Na^+ disorder. They proposed that the formed defective energy levels could act as electron capture centers, facilitating energy transfer from the traps to the Eu^{2+} and thus suppressing the loss of non-radiative transition[25]. They further achieved the regulation of negative to zero thermal TQ by partially replacing Sc^{3+} with Lu^{3+} in NSP: Eu^{2+} while preserving the original high emission efficiency[26]. They correlated the variation of TQ behavior with the reduced Na^+ conductivity (increased migration barrier) and trap concentration. Since there is not always trap-related thermal luminescence in ion conductors synthesized under non-reductive atmospheres, as far as available previous research is concerned[27], a clear relationship between dynamic defects/ions and the TQ behavior is yet absent. Herein, the dynamic defects/ions are defined as a kind of species composed of swapping ion and vacancy in a dynamic equilibrium state.

While the broadband emission of Eu^{2+} ion owing to *d-f* transition is too sensitive to chemical environment variation around Eu^{2+}, *f–f* transition with line-shaped emission peak of lanthanide ions with +3 valence is preferred to figure out the relation. Among the lanthanide ions, the Er^{3+} ion is a well-researched object which converts infrared photons to visible light through the UC process due to its proper electronic energy level configuration. The codopant Yb^{3+} ion can remarkably enhance the UC yield due to the efficient energy transfer from Yb^{3+} to Er^{3+}[28]. Furthermore, the ratio between the red and green emission peaks of the Er^{3+} ion has been reported that they can tell the thermal-induced local structure changes concerning ion migration in the ion conductor materials, both in micro view of localized luminescence and macro view of thermodynamics[27,29-31]. Although Eu^{2+} ions occupy Na^+ site[25-26,32] while Yb^{3+}/Er^{3+} ions likely take Sc^{3+} site, the distance of the adjacent species of Na^+(Eu^{2+})-Na^+/Na vacancy and Sc^{3+}(Yb^{3+}/Er^{3+})-Na^+/Na vacancy are almost equivalent, i.e., 3.4 and 3.2 Å (COD No. 1539810), respectively. The thermal-activated motion of Na^+/Na vacancy should impact the luminescence of Eu^{2+}/Er^{3+} in a similar way but to a different extend. Therefore, we choose the Yb^{3+}/Er^{3+} doped NSP, with excellent optical probe properties, to investigate the correlation of thermally accelerated dynamic defects/ions and distinct thermal quenching of UC and DS luminescence, aiming to find some common clues concerning the ionic conductor type host with good thermal quenching of luminescence. The temperature-dependent X-ray diffraction (XRD), Raman spectroscopy, laser thermal conductivity, photoluminescence (PL) and PL decay curves, alternating current (AC) impedance spectroscopy, and theoretical calculations were

performed to reveal it.

2 Experiment

2.1 Materials and Synthesis.

The $Na_3Sc_2(PO_4)_3$: 0.28Yb^{3+}, 0.04Er^{3+} was synthesized through a traditional high-temperature solid-state reaction. Stoichiometric amounts of Na_2CO_3 (99.99%), Sc_2O_3 (99.99%), $NH_4H_2PO_4$ (99.99%), Yb_2O_3 (99.99%), and Er_2O_3 (99.99%) were mixed and ground in an agate mortar. The mixture was calcined in a muffle furnace at 473 K for 2 hours and then at 1573 K for 12 hours with intermediate grinding. The NSPYE powder and a poly(vinyl alcohol) binder solution were thoroughly mixed, pressed under 10 MPa pressure, and finally sintered at 1573 K to obtain sintered ceramic pellets. We prepared about 20 grams of the sample.

2.2 Material Characterization.

The phase structure at room temperature was determined using a Panalytical X'pert PRO diffraction diffractometer with a PIXcel 1D detector using Cu Kα radiation. Temperature-dependent XRD measurements were performed under vacuum using an Anton Parr HTK 1200N high-temperature attachment over the 10-100° 2θ range. Hold for 3 minutes at each set temperature point, then collect data for another 5 minutes. The laser confocal Raman spectrometer (RENISHAW), equipped with a high-temperature attachment (Instec), was used to record temperature-dependent Raman spectra. The morphology and element distribution of the sample were detected using a scanning electron microscope (JSM-7900F) and an energy-dispersive spectrometer (EDS, JSM-7900F). Temperature-dependent UC and DS emission spectra were recorded on a Horiba JOBIN YVON iHR 320 spectrofluorometer equipped with a high-temperature attachment (Instec). The decay curves were recorded with a Horiba JOBIN YVON iHR 320 spectrofluorometer and an oscilloscope (Tektronix MDO32), using a modulated continuous-wave 980 nm laser as the excitation source. Thermoluminescent measurement was performed using a TOSL-3DS thermoluminescence dosimeter (RongFan Tech), and testing temperature is from room temperature to 773 K with a ramp rate of 1 K/s. The sample was illuminated by a 254 nm lamp for 1 minute before the measurement. A Solartron 1260 A impedance/gain-phase analyzer was used to record the temperature-dependent impedance spectroscopy of ceramic pellet sample over a frequency range of 10^{-1}-10^7 Hz from room temperature to 873 K in the air. The ceramic pellet is coated with gold paste on both sides and then held at 873 K for 2 hours in the air to obtain the electrodes. The thermal diffusivity and heat capacity were obtained by a commercial laser flash apparatus (LFA 427, Netzsch), and the thermal conductivity was calculated by multiplying them by the density of the ceramic pellet. The density can be measured by Archimedes' liquid immersion method before the measurement. The infrared thermography is conducted on a Fotric 225s camera with Fotric AnalyzIR professional infrared thermography analysis software, detecting temperature range of -10 ℃ ~ 350 ℃ and temperature accuracy of ±1.5 ℃.

2.3 Computational Details.

Molecular dynamics (MD) embedded in the MedeA & VASP package was performed to calculate the pair distribution function, the energy fluctuation, and the temperature fluctuation. This simulation is based on density functional theory and the GGA-PBE exchange-correlation function for describing the interactions. The structure model is adopted from the Crystallography Open Database (COD 1539810). Geometry optimization was firstly conducted. A planewave cutoff energy is 300 eV, and the electronic iterations convergence is 1×10^{-4} eV using the Normal (blocked Davidson) algorithm and real space projection operators. The requested k-spacing is 1 Å^{-1}, which leads to a 1×1×1 mesh. This corresponds to actual k-spacing of 0.822×0.823×0.283 Å^{-1}. The k-mesh is forced to be centered on the gamma point. The annealing of the optimized model was simulated via MD (isothermal-isobaric ensemble, nPT) from 298 K to 900 K. The simulation time is 1000 fs with a time step of 4 fs. Then a low-temperature (~317 K) phase structure was extracted from above annealing process, and annealed via MD (canonical ensemble, nVT). The electronic itera-

tions convergence is 1×10^{-3} eV using the Normal (blocked Davidson) algorithm and real space projection operators. The k mesh is also 1×1×1. The simulation time is 1000 fs with a time step of 4 fs, and the simulation temperature ranges from 317 K to 317 K. For the high-temperature (~900 K) phase extracted from MD (nPT) simulation, it was annealed via MD (canonical ensemble, nVT) from 900 K to 900 K. All the other settings are the same.

3 Results and Discussion

3.1 Phase and Structure

It is widely reported that the NSP exists in three crystal structures (α, β, and γ phases), depending on the synthesis conditions and ionic substitution schemes[32]. The α phase is a monoclinic structure with a space group *C2/c*, while the β and γ phases have a hexagonal structure. Phase transition from α *to* β and then to γ would take place with elevated temperature. Interestingly, they all possess a rigid structural framework composed of two ScO_6 octahedra separated by three PO_4 tetrahedra via corner-sharing O atoms, with voids partially occupied by Na^+ ions. Apparently, the difference among these polymorphs lies in the order-disorder degree of Na^+ ions and vacant Na^+ sites (Fig. 1(c)). A scanning electron microscopy (SEM) image of the sample (Fig. 1(d)) displays an irregular crystal morphology with particle size ranging from several to tens of micrometers. Energy-dispersive spectroscopy (EDS) suggests an even distribution of Yb and Er elements (Fig. S1). Variable phases can lead to significant differences in thermal, optical, and electrical properties. Therefore, it is necessary to determine the effect of Yb^{3+}/Er^{3+} dopants on the phase structure and the optimal dopant contents for the subsequent study. A series of samples with gradually increased Yb^{3+}/Er^{3+} contents were synthesized to investigate the phase evolution (Fig. 1(a)). One can see that the NSP experiences an $\alpha\rightarrow\beta$ phase transition with the increase of Yb^{3+}/Er^{3+} amounts. It completely transforms into the β phase when the dopant amount (x + y) is equal to 0.30, with the featured peaks in the enlarged views at 19.8° and 30.8°[32]. Raman spectroscopy is a powerful tool to verify the phases[22]. A split in the stretching modes in the range of 900-1200 cm^{-1} is assigned to the low symmetry monoclinic α phase. The Raman spectra in Fig. S2 confirm the $\alpha\rightarrow\beta$ phase transition. The sample with x = 0.28 and y = 0.04 was selected to conduct follow-up measurements to exclude the possible interference of some minor α phase. The XRD refinement pattern of NSP: $0.28Yb^{3+}$, $0.04Er^{3+}$ (NSPYE) at 298 K is shown in Fig. 1(b), which is consistent with β phase, indicating that it is a pure phase with a space group *R−3c*. The refined results of NSPYE at 298 K are listed in Table S1.

The temperature-dependent XRD data were recorded to determine the phase variation of a β phase NSPYE with elevated temperature (Fig. 2(a)). Although the structures of β and γ phases are similar, the distinct difference between the two diffraction peaks at ~19.5° and the gradual merging of the two diffraction peaks into one diffraction peak at ~ 31° confirm the β to γ phase transition (as seen in the enlarged views of Fig. 2(a)). The lattice parameters obtained from refined temperature-dependent XRD data are shown in Fig. 2(b) and 2(c), which show thermal expansion throughout the testing temperature range. Moreover, the significant different behaviors in the low-temperature and high-temperature regions suggest that NSPYE is a pure β phase below ~448 K and γ phase above ~648 K. There should be coexistence of these two phases at 448~648 K, which is suggested by the following Raman, thermal conductivity, optical and electrical data. Temperature-dependent Raman spectra shown in Fig. 2(d) give some evidence of phase transition. The stretching vibration of PO_4^{3-} group in the range of 900-1200 cm^{-1} doesn't exhibit a splitting feature of the low symmetric monoclinic α phase, indicating the absence of α phase in the synthesized NSPYE. The evolution of β to γ phase is ascertained by fitting the full width at half maximum (FWHM) of the PO_4^{3-} stretching vibration peak. As depicted in Fig. 2(e), the FWHM decreases significantly up to 473 K and then slightly increases afterward. It indicates that the structure experiences a change at ~473 K corre-

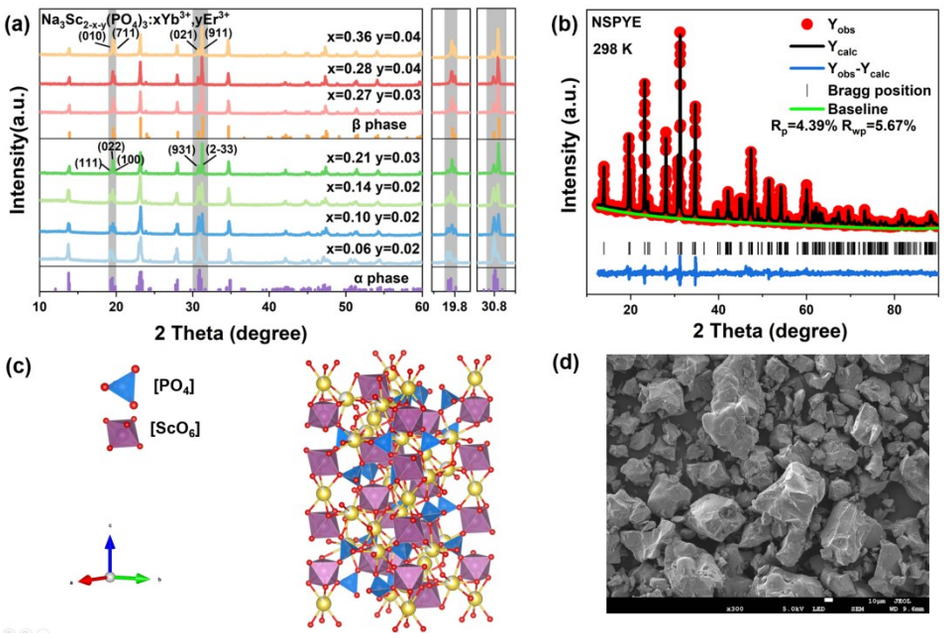

Fig.1 (a)XRD patterns of NSP with increased Yb^{3+}/Er^{3+} contents, the right panel are the enlarged views at ~19.8° and 30.8°.(b) Rietveld refinement result of the XRD pattern of NSPYE at 298 K.(c)Crystal structure of hexagonal NSP.(d)Typical SEM image of NSPYE.

lated to the phase transition from β to γ. The laser thermal conductivity measurement results also ensure the phase transition with rising temperature (Fig. 2(f)). Normally, the enhanced phonon scattering at elevated temperature causes a decrease in thermal conductivity, but the increase of thermal conductivity K in Fig. 2(f) could be understood by the following formula. It consists of two contributions in nonmetallic materials and can be expressed by[33]:

$$K = K_L + K_I \quad (1)$$

where K_L denotes the lattice contribution (phonon transport), K_I denotes the contribution arising from ionic migration and can be further expressed by[33]:

$$K_I = \sigma \times T \times L_I \quad (2)$$

where σ is the ionic conductivity, T is the temperature, L_I is "ionic Lorentz number" deduced from the Sommerfeld Lorentz number. Although K_L follows the law of $K_L \propto T^{-1}$, K_L decreases as the temperature rises, K_I would compensate the K. Herein, ion migration could contribute to the thermal transport, resulting in an increased thermal conductivity. The ion migration will be evidenced by the following optical and electric data.

3.2 Temperature-dependent PL properties

The temperature-dependent UC emission spectra of NSPYE under excitation of a 980 nm laser are shown in Fig. 3(a). The spectra exhibit characteristic green and red emission peaks of Er^{3+} assigned to the ($^2H_{11/2}$, $^4S_{3/2}$) → $^4I_{15/2}$ and $^4F_{9/2}$ → $^4I_{15/2}$ transitions, respectively. As temperature increases from 303 to 873 K, a significant enhancement of green emission (520 + 545 nm) was detected, while the red emission (650 nm) decreases first and then increases. The temperature-dependent DS emission spectra of NSPYE under the 980 nm laser excitation are given in Fig. 3(b). The characteristic near-infrared emission at 1530 nm originates from the $^4I_{13/2}$ → $^4I_{15/2}$ transition of Er^{3+}. To give a clear trend, the normalized integral intensities versus temperature are plotted in Fig. 3(c). When the temperature increases from 303 to 473 K, the green emission intensity slightly increases, while the red and NIR emission intensities decrease. As for the total UC (green + red) emission intensity, it declines. In the temperature range of 473 to 673 K, the red emission intensity weakly changes, while the green emission intensity continues to increase, contributing to the slightly increased total UC emission intensity. The NIR

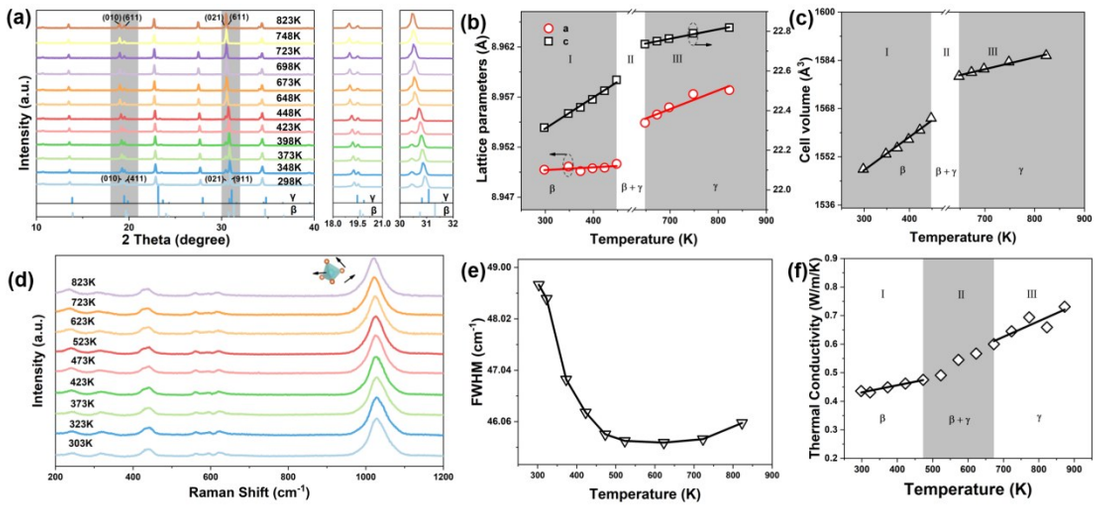

Fig.2 (a) Temperature-dependent XRD patterns of NSPYE and the enlarged views near 19.5° and 31°. Refined temperature-dependent (b) lattice parameters and (c) cell volume. Temperature-dependent (d) Raman spectra and (e) FWHM of the PO_4 stretching vibration mode (located at ~1020 cm^{-1}) of NSPYE. (f) Variation of thermal conductivity of NSPYE with elevated temperature.

emission intensity gradually increases in this temperature range but is still lower than the initial intensity. Above 673 K, interestingly, the green and red emission intensities experience an explosive increase with an enhancement factor of 24.5 and 2.6 at 873 K, respectively. The total UC emission intensity is enhanced by 4.5-fold, while the NIR emission intensity is stable and doesn't show any increase. The evident difference in luminescence thermal enhancement between UC and DS is interesting, and the underlying mechanism will be discussed exhaustively in the following section. In addition, thermoluminescence spectroscopy data of NSPYE (Fig. S3) shows that there is no peak in the TL curve up to 773K, and the sharp rise in TL intensity after 700 K is due to the blackbody radiation, which indicating that the thermal enhancement of NSPYE luminescence has little to do with the trap energy level in this temperature range.

To diminish the minor factors influencing the intensity in addition to the structure variation, we further deal with the UC emission intensity data in integral intensity ratios. The integral intensity ratio between the red and green emissions of the Er^{3+} ion can tell the thermal-induced local structure changes owing to ion/vacancy migration as previous work reported, which is evidenced by various techniques and can be understood by the Judd-Ofelt theory and thermodynamics[27,29-30,34-35]. The logarithm of the integral intensity ratio of the $^2H_{11/2}$ and $^4S_{3/2}$ levels of Er^{3+} linearly changes versus the inverse of the temperature owing to the two thermally-coupled energy levels satisfying Boltzmann's law, which is the basis of optical temperature sensing applications[36]. The method was learned to obtain Fig. 3(d) by plotting the logarithm of the intensity ratio of the emission bands (I_{520}/I_{545} and $I_{520+545}/I_{650}$) versus the inverse of the temperature. It can be observed that two obvious break points locate at ~473 K and ~673 K, respectively. It is inferred that the behaviors below 473 K, above 673 K, at 473~673 K should be assigned to β phase, γ phase and coexistence of these two phases according to the above-discussed phase transition. To figure out the thermal effect of laser irradiation, infrared thermography of NSPYE sample upon 980 nm laser irradiation with a pumping power density of 2.6 W/cm^2 at various temperature are recorded and shown in Figs. S4(a)-(d). It could give a rise of ~ 50 K upon laser irradiation. That is why the breakpoint in temperature-dependent emission behavior deviates from all the other temperature-dependent data. However, the deviation caused by the thermal effect is still acceptable for studying the trend in a wide temperature range from room temperature to 870 K.

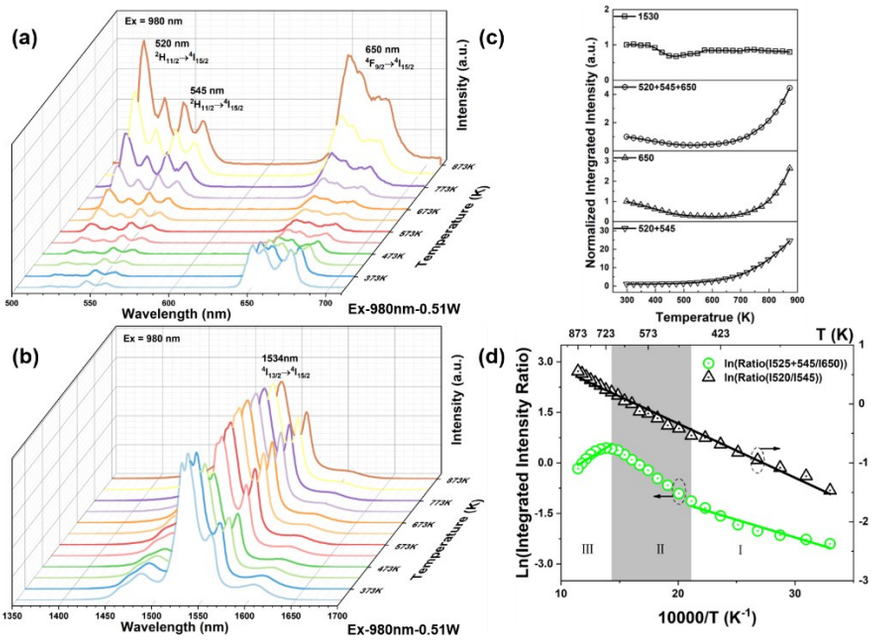

Fig.3 Temperature-dependent(a)UC and(b)DS emission spectra of NSPYE under the excitation of a 980 nm laser, the pumping power density is about 2.6 W/cm^2.(c)Normalized UC and DS emission integral intensities of Er^{3+} in NSPYE.(d)Logarithmic plots of the intensity ratios vs the inverse of absolute temperature.

In the Yb^{3+}/Er^{3+} co-doped phosphors, Yb^{3+} not only acts as radiation-trapping to store energy but also a sensitizer to transfer the energy to Er^{3+}. The contribution of energy transfer(ET) from the sensitizer(Yb^{3+})to the activator(Er^{3+})is essential for achieving efficient UC and DS luminescence of Er^{3+}[37]. Accordingly, the temperature-dependent lifetimes of Yb^{3+} in Yb^{3+}/Er^{3+} co-doped and Yb^{3+} single-doped NSP were measured(Figs. S5(c)and(d)), and the fitted lifetimes are given in Fig. 4(c). The excited state($^2F_{5/2}$ level) lifetimes of Yb^{3+} in Yb^{3+} single-doped NSP are longer than that of Yb^{3+}/Er^{3+} co-doped sample at the same temperature due to the lack of ET from Yb^{3+} to Er^{3+}. The temperature-dependent lifetimes of Yb^{3+} in Fig. 4(c)can be divided into three regions. Region I is when the temperature is below 473 K, i. e., the sample is β phase. The lifetimes of Yb^{3+} in single-doped and co-doped NSP are stable, indicating the increased radiative probability should be nearly equal to the increased nonradiative transition probability of the $^2F_{5/2}$ level of Yb^{3+} with elevated temperature. In region II(temperature between 473 K and 673 K), the sample is a mixture of β and γ phases. However, in region III(above 673 K, γ phase), the lifetime of Yb^{3+} in single-doped NSP slightly declines while it significantly increases in Yb^{3+}/Er^{3+} co-doped sample of NSPYE. It is most likely due to complex energy transfer processes between Yb^{3+} and Er^{3+}. Notably, the lifetime of the $^2F_{5/2}$ level of Yb^{3+} in NSPYE in Fig. 4(c)is stable in region I, but increases sharply in region III, resulting in a slow rise in region II for the mixture of two phases.

To figure out the underlying mechanism of the distinct difference in luminescence thermal enhancement between UC and DS, the temperature-dependent lifetimes of the $^4S_{3/2}$ and $^4I_{13/2}$ levels of Er^{3+} were calculated based on the decay curves(Figs. 4(a)and(b)and(d)). Fig. S5(a)and(b)are partial enlargement of these decay curves focusing on rise stage. It can be seen that the population process of UC slows down with increasing temperature, and it hardly saturate at elevated temperature in a constant pulse width. Below 673 K, one can see that the lifetime of the $^4S_{3/2}$ level can be almost unaffected by elevated temperature, whereas the lifetime of the $^4I_{13/2}$ level decreases and then increases due to thermally induced β to γ phase transition. When the temperature exceeds 673 K, a significant increase in the lifetime of the $^4S_{3/2}$ level can be observed. Nevertheless, the lifetime of the $^4I_{13/2}$ level exhibits a tiny decrease,

deducing that the $^4I_{13/2} \rightarrow {}^4I_{15/2}$ nonradiative transition is promoted. It is unusual to see such a difference in the temperature-dependent UC and DS lifetimes[38-39]. A crucial factor of the significantly slower UC process than the DS process may be the underlying cause (an abstract schematic about electron population rate of slow UC and fast DS is given by Fig. 4 (e)). Rate equations are discussed here to understand the aforementioned slow UC and fast DS process. For clarity, only the 7 main related energy levels of Er^{3+} and a energy level of Yb^{3+} are considered, as shown in the Fig. 4(e). The whole calculation process only considers the two-photon process, the energy transfer between Er^{3+}-Er^{3+} and the back energy transfer of Er^{3+}-Yb^{3+} ions and the loss of UC luminescence are not considered[4,40]. It seems to be reasonable since the fast nonradiative multiphonon relaxation from the $^4I_{11/2}$ to the $^4I_{13/2}$ level greatly reduces the back-energy transfer from Er^{3+}: $^4I_{11/2}$ to Yb^{3+}: $^2F_{7/2}$. The ignored UC loss could be rationalized by the large energy gap for the UC luminescence. More importantly, it is a simplified model balancing the complexity and feasibility to be dealt with. The rate equations concerning DS and UC of green emission are as follows[34,41-42]:

$$\frac{dN_2}{dt} = k_1 N_8 + W^{NR}_{(3\rightarrow 2)} N_3 - k_2 N_2 - W_2 N_2 \# \quad (3)$$

$$\frac{dN_6}{dt} = k_1 k_3 N_3 N_8 + W^{NR}_{(7\rightarrow 6)} N_6 - W^{NR}_{(6\rightarrow 5)} N_6 - W_6 N_6 \# \quad (4)$$

$$\frac{dN_7}{dt} = k_1 k_3 N_3 N_8 - W^{NR}_{(7\rightarrow 6)} N_7 - W_7 N_7 \# \quad (5)$$

where N_i (i=1, 2, 3, 4, 5, 6 and 7) is the population density of the $^4I_{15/2}$, $^4I_{13/2}$, $^4I_{11/2}$, $^4I_{9/2}$, $^4F_{9/2}$ (red emission), $^4S_{3/2}$ and $^2H_{11/2}$/$^4F_{7/2}$ (green emission) levels of Er^{3+}, respectively, N_8 is the population density of the $^2F_{5/2}$ level of Yb^{3+}. W_i represents the radiative transition coefficient. $W^{NR}_{(i\rightarrow j)}$ denotes the depopulation coefficient due to non-radiative decay from the i level to the j level. $k_{1or2or3}$ represents the energy transfer coefficient of the three UC processes. Under steady-state excitation, the resident time of excited electron at $^4I_{13/2}$ level is long, and the non-radiative decay coefficient $W^{NR}_{(3\rightarrow 2)}$ is always high and even higher at elevated temperature[38], contributing to the fast DS population process. However, the UC population (equation 4 and 5) is closely correlated to the product of energy transfer coefficient k_1k_3. The k_1k_3 may be primarily determined by the product of decay lifetimes of two intermediate excited states involved in green UC process[42]. It could be largely influenced by the separation distance r between Yb^{3+} and Er^{3+} since the energy transfer rate is proportional to r^n (n=-6 for the electric dipole-electric dipole interaction model)[43-44], and resident time of quenching centers of defects around rare earth ions (impacts decay lifetimes). When r increases (as cell parameters behave in Fig. 2(b) and (c)) and resident time of defects around Yb^{3+}/Er^{3+} reduces (as deduced and discussed in the following section) with elevated temperature, the product of k_1k_3 would apparently decline. It results in a slower UC population process. The UC and DS luminescence exhibit significant differences in thermal enhancement at high temperatures (above 673 K). It suggests that the slow UC population process is more susceptible to dynamic ions/defects motion than the fast DS population process in the perspective of ET. In addition, we deduce that the dynamic ions/defects in ion-conductive NSPYE are likely no longer the TQ center, considering the resident time near Yb^{3+}/Er^{3+} sites as discussed in the following sections. Notice, the effect of refractive index variation on spontaneous emission probability and energy transfer coefficient is still unknown in NSPYE since it is hard to measure the temperature-dependent refractive index for the powder sample. According to some literatures[45-46], the variation should be extreme small for the second-order phase transition with constant composition. Furthermore, there are always other factors to influence spontaneous emission probability and energy transfer coefficient, making it difficult to distinguish the effect of refractive index variation.

3.3 Temperature-dependent AC impedance and simulation

Temperature-dependent AC impedance spectroscopy measurements were carried out on the NSPYE ceramic pellet to prove the abovementioned

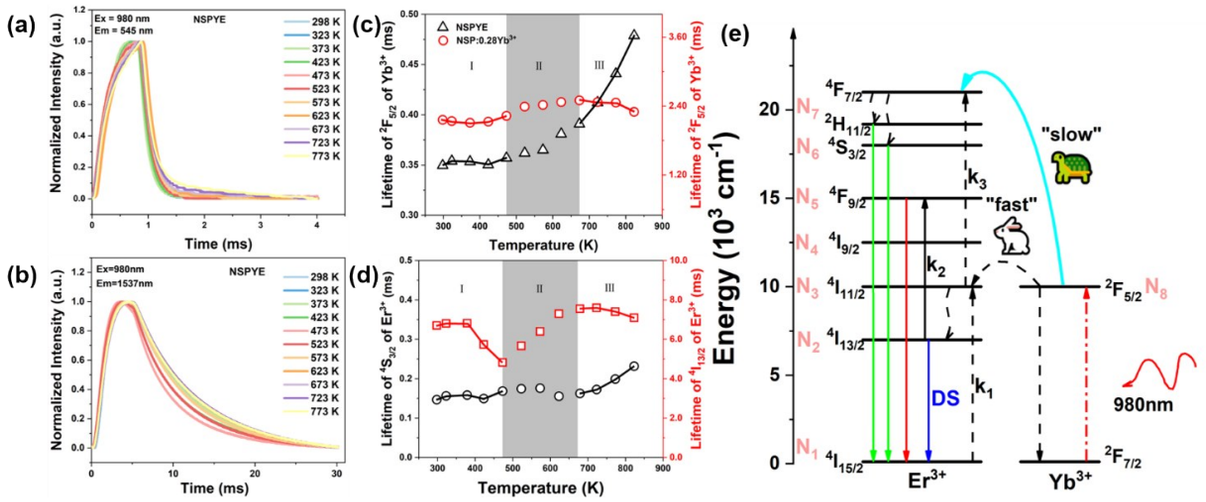

Fig.4 Temperature-dependent decay curves of(a) the $^4S_{3/2}$ level and(b) $^4I_{13/2}$ level of Er^{3+} under the 980 nm laser excitation.(c) Temperature-dependent lifetimes of the $^2F_{5/2}$ level of Yb^{3+} in Yb^{3+}/Er^{3+} co-doped and Yb^{3+} single-doped NSP.(d) Temperature-dependent lifetimes of the $^4S_{3/2}$ and $^4I_{13/2}$ levels of Er^{3+} in NSPYE.(e) Energy level diagram of UC and DS emission showing the proposed temperature-dependent electronic transition and energy-transfer processes in NSPYE.

deduction. The typical complex impedance data of NSPYE ceramic pellet at 373 K in air comprise two semicircular arcs in the high-frequency region and one tail in the low-frequency region (Fig. 5(a)). The first semicircular arc can be modeled with an equivalent circuit consisting of parallel resistor(R) and capacitor(C) components. The intercept of the first semicircular arc in high frequency was extracted as bulk resistance. The tail in the low-frequency region implies the Na^+ ions migration-related electrode responses. The Arrhenius plot for bulk conductivity of NSPYE is shown in Fig. 5(b). In the low-temperature region(β phase), the activation energy of the Na^+ migration is ~0.52 eV, while in the high-temperature region it shows much higher ionic conductivity (γ phase) with the activation energy 0.29 eV(673 K-873 K). Once again, we can see that the slope in the region II is roughly the median of slopes of the region I and region III. Ascribing to the similar structure of β and γ phases and different sensitivities of various properties to structure, it is necessary to take all the variable-temperature properties into account to determine the transition region with the mixture of two phases. The decreased activation energy in γ phase corresponds to the region III in Fig. 3(d). The pair distribution functions of NSP simulated via DFT calculation at 300 K and 900 K indicate that Na^+ ion is more active at high temperature(Figs. 5(c) and(d)). The total energy and temperature fluctuation of NSP at 300 K and 900 K are shown in Figs. 5(e) and(f), respectively. One can see that the amplitude of temperature fluctuations of NSP at 900 K is more dramatic than that at 300 K, implying larger probability of ions/defects jumping. Suppose that the Na^+ ions are located at the nearest neighbored sites around Yb^{3+}/Er^{3+}, the jumping probability of Na^+ ions(p, i. e., the probability of a thermal fluctuation energy larger than activation energy ε)to a nearby vacancy upon thermal fluctuations can be expressed by[34,47-48]:

$$p = e^{-\varepsilon/kT} \tag{6}$$

where k is the Boltzmann constant, and T is the absolute temperature. The obtained activation energy data in Fig. 5(b) were used to calculate the Na^+ ions jumping probability, which are 10^{-8} at 300 K and 10^{-3} at 700 K, respectively. It indicates that the jumping probability of Na^+ ion/vacancy at high temperature is much larger than at low temperature. If we take the atomic vibration frequency as 10^{12} Hz, the jumping frequency of the Na^+ ion/vacancy could be 10^4 at 300 K and 10^9 Hz at 700 K, respectively. That is, the Na^+ ion/vacancy would stay at the nearest neighbored sites around Yb^{3+}/Er^{3+} ions for about 10^{-4} s at 300 K and 10^{-9} s at 700 K, respectively. The dura-

tion time of a UC process is significantly longer than that of a DS process. The relative slow process of Na^+/vacancy swapping would impose less effect on a fast DS process, while time scale of swapping process is equivalent to that of the UC process. In other words, the dynamic Na^+ ion/vacancy in ion-conductive NSPYE at high temperature no longer acts as the TQ center in the slow UC process[27].

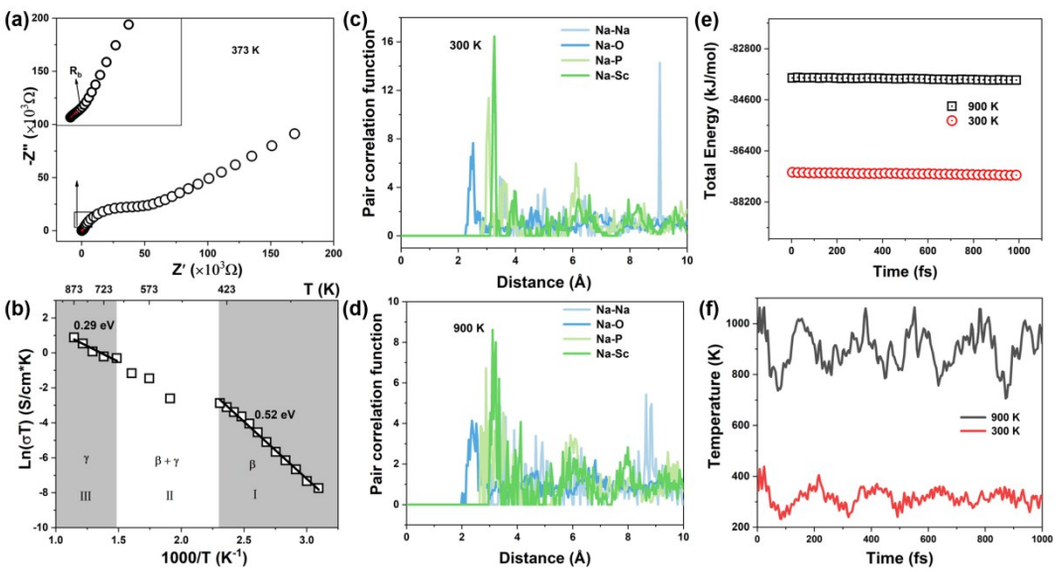

Fig.5 (a) Impedance spectrum of NSPYE at 373 K. (b) Arrhenius plot of the bulk conductivity of the NSPYE ceramic pellet at 323–873 K. Pair distribution functions of NSP at (c) 298 K and (d) 900 K. (e) Total energy and (f) temperature fluctuation of NSP with increased time at 300 K and 900 K.

Since the jumping process of Na^+ ions upon thermal activation is similar to the process of Brownian motion, a classical diffusion model is used to estimate the jumping distance of Na^+, in which the jumping distance d is deduced by[30,47]:

$$\sigma = \frac{n_0 e^2}{kT} v_0 d^2 e^{-\frac{\varepsilon}{kT}} \tag{7}$$

where σ and ε represent the ionic conductivity and the corresponding activation energy, respectively; n_0 is the number of ions that can migrate per unit volume, ν_0 is the vibration frequency of the ions, e is the unit charge, k is the Boltzmann constant, and T is the absolute temperature.

Since both two Na^+ sites are partially and disorderedly occupied, we take the distance between two adjacent Na^+ sites (~3.40 Å, adopted from COD No. 1539810) as the jumping distance of Na^+ ion to the adjacent Na^+ site vacancy. Then the calculated content of transported defect (Na^+) is ~4 defects (ions) per unit cell volume of 1537 $Å^3$ for 367 K with the fitted activation energy of 0.52 eV (data adopted from Fig. 5(b)). The value is reasonable with reference to the case of all Na^+ ions contributed to ionic conductivity (n_0 is 18 ions per unit cell volume of 1537 $Å^3$ according to COD No. 1539810, then d is calculated to be 5.36 Å for 367 K).

According to the above data and discussion, we try to give a complete picture concerning the dynamic defects/ions, NTQ of UC luminescence, and the thermal stability of DS luminescence. When the temperature is below 473 K (β phase), the UC and DS emissions are mainly controlled by the competed radiative and nonradiative transition. Between 473 K and 673 K, the sample is a mixture of β and γ phases. Above 673 K, thermally accelerated Na^+ ions migration are not TQ centers anymore but instead contributes to the promoted radiative transition and suppressed nonradiative transition, leading to significant NTQ of UC luminescence and thermally stabilized DS luminescence. The distinct difference between UC and DS is mainly due to the difference in population rates for these emitting levels. The slow UC process should be more easily perturbed by Na^+ ions migration in a longer time scale, contributing to its NTQ luminescence.

4 Conclusion

In summary, a picture concerning the dynamic defects/ions, NTQ of UC luminescence, and the thermal stability of DS luminescence is proposed in NSPYE. The slightly decreased UC and DS emission intensity in β phase is ascribed to the competitive quenching process by static Na^+ defect and ET process. While for γ phase at high temperature, thermally accelerated dynamic defects/ions contributed to the significant NTQ of UC luminescence and thermally stabilized DS luminescence by promoting the radiative transition and suppressing the non-radiative transition. Interestingly, the UC process with slow population rate is more susceptible to perturbation of Na^+ ions migration with jumping frequency in an equivalent time scale, resulting in evident NTQ luminescence of UC. This research not only opens an avenue for understanding the NTQ mechanism of luminescence via the dynamic defects/ions, but also suggests the potential application of NSPYE in high-temperature optical sensing and imaging.

References:

[1] AMACHRAA M, WANG Z B, CHEN C, *et al.* Predicting Thermal Quenching in Inorganic Phosphors [J]. *Chem Mater.*, 2020, 32(14): 6256-65.

[2] BALCI M H, CHEN F, CUNBUL A B, *et al.* Comparative study of blue laser diode driven cerium-doped single crystal phosphors in application of high-power lighting and display technologies [J]. *Opt Rev.*, 2018, 25(1): 166-74.

[3] COZZAN C, BRADY M J, O'DEA N, *et al.* Monolithic translucent $BaMgAl_{10}O_{17}:Eu^{2+}$ phosphors for laser-driven solid state lighting [J]. *AIP Adv.*, 2016, 6(10).

[4] LIU T, YANG Z, XU S. 3-Dimensional heat analysis in short-length Er^{3+}/Yb^{3+} co-doped phosphate fiber laser with upconversion [J]. *Opt Express.*, 2009, 17(1): 235-47.

[5] YOSHIMURA K, ANNEN K, FUKUNAGA H, *et al.* Optical properties of solid-state laser lighting devices using SiAlON phosphor-glass composite films as wavelength converters [J]. *Jpn J Appl Phys.*, 2016, 55(4).

[6] 郑鹏,丁国真,解荣军. Ce^{3+}和Eu^{2+}掺杂荧光材料的光猝灭机理研究进展 [J]. 发光学报, 2021, 42(10): 1447-57.
ZHENG P, DING G Z, XIE R J. Progress on the photo-burst mechanism of Ce^{3+} and Eu^{2+} doped fluorescent materials [J]. *Chin. J. Lumin.*, 2021, 42(10): 1447-57. (in Chinese)

[7] WANG S B, CHEN W B, ZHOU D C, *et al.* Long persistent properties of $CaGa_2O_4:Bi^{3+}$ at different ambient temperature [J]. *J Am Ceram Soc.*, 2017, 100(8): 3514-21.

[8] ZHANG M, XIA Z, LIU Q. Thermally stable $K_xCs_{1-x}AlSi_2O_6:Eu^{2+}$ phosphors and their photoluminescence tuning [J]. *J Mater Chem C.*, 2017, 5(30): 7489-94.

[9] WEI Y, YANG H, GAO Z, *et al.* Anti-thermal-quenching Bi^{3+} luminescence in a cyan-emitting $Ba_2ZnGe_2O_7:Bi$ phosphor based on zinc vacancy [J]. *Laser Photonics Rev.*, 2021, 15(1): 2000048.

[10] SHI R, NING L, WANG Z, *et al.* Zero-Thermal Quenching of Mn^{2+} Red Luminescence via Efficient Energy Transfer from Eu^{2+} in $BaMgP_2O_7$ [J]. *Adv Opt Mater.*, 2019, 7(23).

[11] KIM Y H, KIM H J, ONG S P, *et al.* Cation-Size Mismatch as a Design Principle for Enhancing the Efficiency of Garnet Phosphors [J]. *Chem Mater.*, 2020, 32(7): 3097-108.

[12] Y-TTSAI, C-YCHIANG, ZHOU W, *et al.* Structural Ordering and Charge Variation Induced by Cation Substitution in $(Sr,Ca)AlSiN_3:Eu$ Phosphor [J]. *J Am Chem Soc.*, 2015, 137(28): 8936-9.

[13] WEI Y, CAO L, LV L, *et al.* Highly Efficient Blue Emission and Superior Thermal Stability of $BaAl_{12}O_{19}:Eu^{2+}$ Phosphors Based on Highly Symmetric Crystal Structure [J]. *Chem Mater.*, 2018, 30(7): 2389-99.

[14] ZHAO D, XUE Y-L, ZHANG S-R, *et al.* Non-concentration quenching, good thermal stability and high quantum efficiency of $K_5Y(P_2O_7)_2:Eu^{3+}/Tb^3$+ phosphors with a novel two-dimensional layer structure [J]. *J Mater Chem C.*, 2019, 7(45): 14264-74.

[15] ZOU H, CHEN B, HU Y, *et al.* Simultaneous Enhancement and Modulation of Upconversion by Thermal Stimulation in Sc_2-Mo_3O_{12} Crystals [J]. *J Phys Chem Lett.*, 2020, 11(8): 3020-4.

[16] ZOU H, YANG X, CHEN B, *et al.* Thermal Enhancement of Upconversion by Negative Lattice Expansion in Orthorhom-

bic $Yb_2W_3O_{12}$ [J]. *Angew Chem, Int Ed.*, 2019, 58(48): 17255-9.

[17] HUANG P, ZHOU B, ZHENG Q, *et al.* Nano wave plates structuring and index matching in transparent hydroxyapatite-YAG: Ce composite ceramics for high luminous efficiency white light-emitting diodes [J]. *Adv Mater.*, 2020, 32(1): 1905951.

[18] ZHU Y, LIANG Y, LIU S, *et al.* Design of hierarchical composite silicate for full-color and high thermal stability phosphors [J]. *Chem Eng J.*, 2018, 345: 327-36.

[19] PIAO S, WANG Y, ZHOU X, *et al.* Defect Engineering in a Eu^{2+}-Doped β-Al_2O_3 Structure Blue Phosphor and Its Controllable Zero-Thermal Quenching Luminescence [J]. *ACS Sustainable Chem Eng.*, 2021, 9(23): 7882-90.

[20] LIN C C, LIU R-S. Advances in Phosphors for Light-emitting Diodes [J]. *J Phys Chem Lett.*, 2011, 2(11): 1268-77.

[21] TAKEDA T, HIROSAKI N, FUNAHSHI S, *et al.* Narrow-Band Green-Emitting Phosphor $Ba_2LiSi_7AlN_{12}$:Eu^{2+} with High Thermal Stability Discovered by a Single Particle Diagnosis Approach [J]. *Chem Mater.*, 2015, 27(17): 5892-8.

[22] COLLIN G, COMES R, BOILOT J P, *et al.* Disorder of tetrahedra in Nasicon-type structure—I.: $Na_3Sc_2(PO_4)_3$: Structures and ion-ion correlations [J]. *J Phys Chem Solids.*, 1986, 47(9): 843-54.

[23] SUSMAN S, DELBECQ C J, BRUN T O, *et al.* Fast ion transport in the NASICON analog $Na_3Sc_2(PO_4)_3$: structure and conductivity [J]. *Solid State Ion (Netherlands).*, 1983, 9-10(2): 839-44.

[24] WANG X, ZHAO Z, WU Q, *et al.* Structure, photoluminescence and abnormal thermal quenching behavior of Eu^{2+}-doped $Na_3Sc_2(PO_4)_3$: a novel blue-emitting phosphor for n-UV LEDs [J]. *J Mater Chem C.*, 2016, 4(37): 8795-801.

[25] KIM Y H, ARUNKUMAR P, KIM B Y, *et al.* A zero-thermal-quenching phosphor [J]. *Nat Mater.*, 2017, 16(5): 543-50.

[26] VISWANATH N S M, FANG M-H, HUU H T, *et al.* Correlated Na^+ Ion Migration Invokes Zero Thermal Quenching in a Sodium Superionic Conductor-type Phosphor [J]. *Chem Mater.*, 2022, 34(1): 107-15.

[27] WANG Y, AN Z, TAO Z, *et al.* Thermodynamics and Kinetics Accounting for Antithermal Quenching of Luminescence in $Sc_2(MoO_4)_3$: Yb/Er: Perspective beyond Negative Thermal Expansion [J]. *J Phys Chem Lett.*, 2022, 13(51): 12032-40.

[28] LIM C S, ATUCHIN V, ALEKSANDROVSKY A, *et al.* Microwave sol – gel synthesis of $CaGd_2(MoO_4)_4$:Er^{3+}/Yb^{3+} phosphors and their upconversion photoluminescence properties [J]. *J Am Ceram Soc.*, 2015, 98(10): 3223-30.

[29] LI Y, JIANG X-F, TAO F-Q, *et al.* Detection of oxide-ion and oxygen vacancy swapping via upconversion luminescence in $La_2Mo_2O_9$: Yb^{3+}, Er^{3+} [J]. *J Mater Chem C.*, 2016, 4(30): 7286-93.

[30] XIONG J, ZHAO Y, ZHU J, *et al.* Optical Interpretation of a Second-Order Phase Transition Induced by Thermal-Driven Li^+ Migration via Configurational Entropy in $CaTiO_3$:Li^+, Yb^{3+}, Er^{3+} [J]. *J Phys Chem C.*, 2021, 125(12): 6916-22.

[31] 熊敬协,朱嘉熙,叶柿. 稀土发光的视角探讨固体中热致离子迁移行为 [J]. 中国稀土学报, 2020, 38(03): 307-25.

XIONG J X, ZHU J X, YE S. A rare-earth luminescence perspective on the behaviour of thermotropic ion migration in solids [J]. *J. Chin. Rare Earth Soc.*, 2020, 38(03): 307-25. (in Chinese)

[32] LIU Z, ZHOU T, YANG C, *et al.* Tunable thermal quenching properties of $Na_3Sc_2(PO_4)_3$:Eu^{2+} phosphors tailored by phase transformation details [J]. *Dalton Trans.*, 2020, 49(11): 3615-21.

[33] RICE M J, ROTH W L. Ionic transport in super ionic conductors: a theoretical model [J]. *J Solid State Chem.*, 1972, 4(2): 294-310.

[34] ZHU J, HE Q, KUANG X, *et al.* An optical perspective on the thermal-activated ionic migration state and ionic jumping distance in glass [J]. *J Mater Chem C.*, 2019, 7(30): 9211-8.

[35] WANG P, WANG Y, TAO Z, *et al.* Photoionic Effect Imposed by Photoresponsive Local Field in a Tellurate Glass with Lanthanide Ions and Ag Nanoparticles [J]. *ACS Appl Mater Interfaces.*, 2023, 15(21): 25704-12.

[36] DOS SANTOS P, DE ARAUJO M, GOUVEIA-NETO A, *et al.* Optical temperature sensing using upconversion fluorescence emission in Er^{3+}/Yb^{3+}-codoped chalcogenide glass [J]. *Appl Phys Lett.*, 1998, 73(5): 578-80.

[37] WANG F, DENG R, WANG J, *et al.* Tuning upconversion through energy migration in core – shell nanoparticles [J]. *Nat Mater.*, 2011, 10(12): 968-73.

[38] SARDAR D K, GRUBER J B, ZANDI B, *et al.* Judd – Ofelt analysis of the Er^{3+} ($4f^{11}$) absorption intensities in phosphate glass: Er^{3+}, Yb^{3+} [J]. *J Appl Phys.*, 2003, 93(4): 2041-6.

[39] PISARSKI W A, PISARSKA J, LISIECKI R, *et al.* Er^{3+}/Yb^{3+} co-doped lead germanate glasses for up-conversion luminescence temperature sensors [J]. *Sens Actuators, A.*, 2016, 252: 54-8.

[40] ZHAO J, LU Z, YIN Y, *et al.* Upconversion luminescence with tunable lifetime in $NaYF_4$:Yb,Er nanocrystals: role of nanocrystal size [J]. *Nanoscale.*, 2013, 5(3): 944-52.

[41] SUYVER J, AEBISCHER A, GARCíA-REVILLA S, *et al.* Anomalous power dependence of sensitized upconversion luminescence [J]. *Phys Rev B.*, 2005, 71(12): 125123.

[42] KONG J, SHANG X, ZHENG W, *et al.* Revisiting the Luminescence Decay Kinetics of Energy Transfer Upconversion [J]. *J Phys Chem Lett.*, 2020, 11(9): 3672-80.

[43] RABOUW F T, DEN HARTOG S A, SENDEN T, *et al.* Photonic effects on the Förster resonance energy transfer efficiency [J]. *Nat Commun.*, 2014, 5(1): 3610.

[44] FöRSTER T. Zwischenmolekulare Energiewanderung und Fluoreszenz [J]. 1948, 437(1-2): 55-75.

[45] AKISHIGE Y, YONEYA Y, OHI K, *et al.* Refractive Index and Birefringence of Sr2Nb2O7 around the Incommensurate Phase Transition [J]. *J Phys Soc Jpn.*, 1989, 58(2): 398-401.

[46] ANDRIYEVSKY B, CZAPLA Z, ROMANYUK M, *et al.* Peculiarities in Thermal Linear Expansion and Refractive Indices of (NH2CH2COOH)·H3PO3 Single Crystals in the Region of Phase Transition [J]. *Phys Status Solidi.*, 2000, 177(2): 575-82.

[47] RICE M J, ROTH W. Ionic transport in super ionic conductors: a theoretical model [J]. *J Solid State Chem.*, 1972, 4(2): 294-310.

[48] LACHARME J P, ISARD J. Ionic jump processes and high field conduction in glasses [J]. *J Non-Cryst Solids.*, 1978, 27(3): 381-97.

汪世杰(1999年-),男,湖南汨罗人,硕士研究生,2021年于长春理工大学获得学士学位,主要从事稀土掺杂无机材料与热致离子迁移的研究。

E-mail:18173017880@163.com

叶柿(1981年-),男,广西昭平人,华南理工大学教授;分别于2004年和2009年获得兰州大学学士学位和北京大学博士学位;主要从事稀土/过渡金属发光材料及其器件化、功能复合化的基础研究,以多角度、多尺度研究材料结构-性能之间的构效关系。

E-mail: msyes@scut.edu.cn